

Towards the Prediction of Flow and Acoustic Fields of a Jet-Wing-Flap Configuration

Daniel Schütz and Holger Foyssi

Abstract Coaxial jets originating from a nozzle interacting with a two-element wing configuration consisting of a main wing and a flap are computed using large-eddy simulations (LES) to investigate in the long term the effect of the interaction on the sound field of this jet-wing-flap configuration. The secondary jet Mach number is $M_s = 0.37$ and the Reynolds number based on the secondary velocity and diameter is $Re_s = 1.32 \times 10^6$. The nozzle inlet boundary layers are modeled by Blasius velocity profiles with a boundary layer thicknesses of 20% of the nozzle channel half-width. The acoustic far-field is predicted by solving the linearized Euler equations (LEE) in a region attached to the LES domain. The jet streams interacts with the two-element wing configuration and lead to a significantly changed mean flow field in the wing-flap gap area and pressure at the wing surface. Additionally, a strong influence of the flap on the jet development is observed, especially in the case of a non-zero free stream velocity.

1 Introduction

Aeroacoustic noise has been investigated intensively during the last decade. Although big progress was made in many areas, there still is further research needed to obtain a better understanding, for example, of jet flows interacting with solid structures or noise emitted by the flow around bodies. Jet flows with higher Reynolds numbers including the nozzle lip geometry were investigated by Xia et al. [22], Bogey et al. [4] and Bühler et al. [5], for example. Andersson et al. [1], Vuillemin et al. [19], Georgiadis and DeBonis [11], Eschricht et al. [7] and Bogey et al. [3] calculated coaxial jets to investigate the differences compared to canonical jet flows. The noise

D. Schütz (✉) · H. Foyssi

Lehrstuhl für Strömungsmechanik, Universität Siegen, Paul-Bonatz-Str. 9-11,
57068 Siegen, Germany
e-mail: daniel.schuetz@uni-siegen.de

H. Foyssi

e-mail: holger.foysi@uni-siegen.de

© Springer International Publishing AG 2018

A. Dillmann et al. (eds.), *New Results in Numerical and Experimental Fluid Mechanics XI*, Notes on Numerical Fluid Mechanics and Multidisciplinary Design 136, https://doi.org/10.1007/978-3-319-64519-3_59

emission of airfoils alone has been investigated by [10, 14, 21] to name a few. However, the described cases don't often occur isolated from each other, as turbines are mounted below wings and the jet flow is interacting with the wing geometry. To address this, a Reynolds-Averaged-Navier-Stokes computation of a generic jet-flap configuration has been conducted by Neitfeld et al. [16]. To predict the sound pressure fluctuations they used the eddy relaxation source model. But for the assessment of acoustical trends, more computations with varying jet-conditions and flap angles would be necessary.

Because of this, the focus of this work is on simulating a jet-wing-flap configuration, with the final goal of investigating the influence of the jet velocity, jet temperature and coflow as well as wing position and flap angle on the spatial distribution and directivity pattern of the acoustic sources.

2 Simulation Parameters

2.1 LES Procedure and Parameters

The numerical framework for the intended LES simulations is based on the open-source package Overture [12]. The compressible Navier-Stokes equations in conservative form $(\rho, \rho \mathbf{u}, E)$ are solved on body-fitted overlapping grids, using 2nd-order central differences for the spatial derivatives and an Adams-Predictor-Corrector method of 2nd or 4th-order in time. The Lagrange interpolation between the grids is explicit and of 4th-order accuracy [6]. Artificial damping is further introduced to prevent spurious waves [12, 13], direct filtering is used as LES model [8]. The computational grid for one of the simulated cases is shown exemplarily in Fig. 1. It is build up using a background grid with $n_x \times n_y \times n_z = 676 \times 401 \times 401$ grid points and two embedded foreground grids for the airfoil, as well as four for the nozzle. Table 1 indicates the relevant parameters. The wing is uniform in spanwise direction

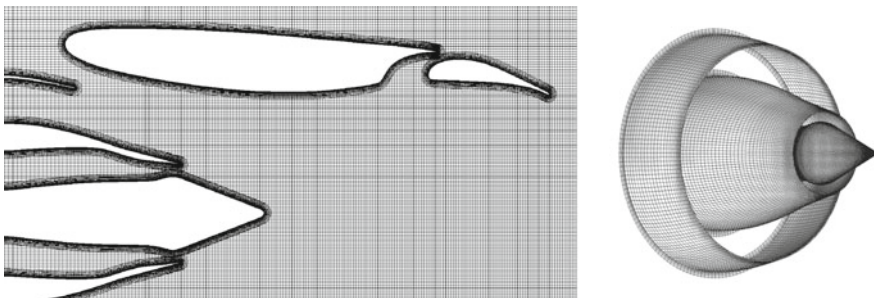


Fig. 1 Simulation grid for the (x, y) -plane at $z = 0$ (left). Surface grid of the 3D nozzle (right). Every third gridpoint is shown

Table 1 Grid parameters. The overline indicates the average value

Grid	$n_s \times n_r \times n_\theta(n_z)$	$\overline{\Delta s}$	$\overline{\Delta r}$	Δr_{\min}	$\overline{\Delta\theta(\Delta z)}$
Wing	$426 \times 15 \times (251)$	$0.0085D_s$	$0.0017D_s$	$0.00064D_s$	$(0.016D_s)$
Flap	$176 \times 15 \times (251)$	$0.0067D_s$	$0.0017D_s$	$0.00064D_s$	$(0.016D_s)$
Nozzle s	$121 \times 15 \times 563$	$0.0065D_s$	$0.0017D_s$	$0.00064D_s$	$0.0055D_s$
Nozzle p	$496 \times 15 \times 551$	$0.0036D_s$	$0.0017D_s$	$0.00064D_s$	$0.0035D_s$
Plug ^a	$246 \times 15 \times 199$	$0.0057D_s$	$0.0017D_s$	$0.00064D_s$	$0.0038D_s$

^aTo avoid singularities at the plug peak a grid patch of size $n_a \times n_b \times n_r = 76 \times 76 \times 15$ is added

and the boundaries are assumed permeable. To suppress unphysical reflections, a numerical sponge layer is added at the outflow and lateral boundaries. All important simulation parameters are depicted in Table 2.

2.2 Definition of the Inlet Conditions

The nozzle consists of a primary nozzle (index p) and a secondary nozzle (index s). At the inlet boundary the velocity profile is set using a laminar Blasius profile. Figure 2 (right) depicts schematically the different profiles at the nozzle inlet. Their components are determined via

$$u_o(r) = u_{po}(r) + u_{so}(r) + u_{\infty o}(r), \quad v_o = w_o = 0, \quad \text{with} \quad (1)$$

$$u_{jo}(r) = \begin{cases} U_{jo}, & \text{if } r'_j < h_{jo} - \delta_{jo} \\ U_{jo} \frac{h_{jo} - r'_j}{\delta_{jo}} \left[2 - 2 \left(\frac{h_{jo} - r'_j}{\delta_{jo}} \right)^2 + \left(\frac{h_{jo} - r'_j}{\delta_{jo}} \right)^3 \right], & \text{else if } h_{jo} - \delta_{jo} \leq r'_j \leq h_{jo} \\ 0, & \text{else} \end{cases}$$

$$u_{\infty o}(r) = \begin{cases} U_{\infty}, & \text{if } r > R + \delta_{\infty o} \\ U_{\infty} \frac{r'_{\infty}}{\delta_{\infty o}} \left[2 - 2 \left(\frac{r'_{\infty}}{\delta_{\infty o}} \right)^2 + \left(\frac{r'_{\infty}}{\delta_{\infty o}} \right)^3 \right], & \text{else if } R \leq r \leq R + \delta_{\infty o} \\ 0, & \text{else} \end{cases}$$

The indices $j = s, p$ indicate the respective nozzle. h_{jo} is defined as the channel half-width and δ_{jo} as the boundary layer thickness at the nozzle inlet, respectively. Furthermore we have

$$r'_j = \sqrt{(r - r_{jo})^2}, \quad r'_{\infty} = \sqrt{(r - R)^2}.$$

Table 2 Reference values, fluid parameters and dimensionless simulation parameters

Parameter	Value	Normalization	Dimensionless value
γ	1.4	1	1.4
\mathcal{R}_g	287.15 J/(kgK)	T_s/U_s^2	$1/(\gamma M_s^2) \simeq 5.107$
$Pr = c_p \mu / k$	0.715	1	0.715
c_p	1.005×10^3 J/(kgK)	T_s/U_s^2	$1/((\gamma - 1)M_s^2) \simeq 17.84$
μ	1.823×10^{-5} kg/(ms)	$1/(\rho_s U_s D_s)$	$1/Re_s = 7.58 \times 10^{-7}$
ρ_∞	1.205 kg/m ³	$1/\rho_s$	1
U_∞	60 m/s	$1/U_s$	0.467
$\delta_{\infty o}$	0.00264 m	$1/D_s$	0.017
T_∞	293.15 K	$1/T_s$	1
$p_\infty = \rho_\infty \mathcal{R}_g T_\infty$	$\simeq 1.01434 \times 10^5$ Pa	$1/\rho_s U_s^2$	$1/(\gamma M_s^2) \simeq 5.1$
$a_\infty = (\gamma \mathcal{R}_g T_\infty)^{1/2}$	$\simeq 343.3$ m/s	$1/U_s$	$1/M_s \simeq 2.67$
D_s	0.15548 m	$1/D_s$	1
ρ_s	1.205 kg/m ³	$1/\rho_s$	1
ρ_{so}	1.205 kg/m ³	$1/\rho_s$	1
U_s	128.5 m/s	$1/U_s$	1
U_{so}	128.5 m/s	$1/U_s$	1
T_s	293.15 K	$1/T_s$	1
T_{so}	293.15 K	$1/T_s$	1
δ_{so}	0.00264 m	$1/D_s$	0.017
$Re_s = \rho_s U_s D_s / \mu$	$\simeq 1.32 \times 10^6$	1	1.32×10^6
D_p	0.06004 m	$1/D_s$	$\simeq 0.386$
ρ_p	1.205 kg/m ³	$1/\rho_s$	1
ρ_{po}	1.259 kg/m ³	$1/\rho_s$	1.045
U_p	108.2 m/s	$1/U_s$	$\simeq 0.842$
U_{po}	34.05 m/s	$1/U_s$	0.269
T_p	293.15 K	$1/T_s$	1
T_{po}	298.38 K	$1/T_s$	1.018
δ_{po}	0.00233 m	$1/D_s$	0.015
c	0.3 m	$1/D_s$	$\simeq 1.93$
$Re_c = \rho_\infty U_\infty c / \mu$	$\simeq 1.19 \times 10^6$	1	$\simeq 1.19 \times 10^6$

The relation of boundary layer thickness to channel half-width is $\delta_{jo}/h_{jo} = 0.2$. The resulting velocity distribution is shown in Fig. 2 (left).

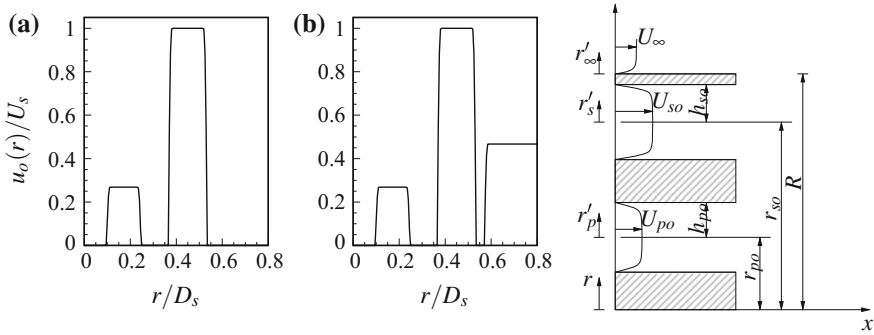


Fig. 2 3D nozzle inlet profiles of the velocity (*left*): **a** without flight-stream **b** with flight-stream. *Right* Schematic illustration of the nozzle inlet

2.3 Verification

To verify the LES procedure various test cases were conducted. As an example, the flow around a two-dimensional NACA0012 profile with angle of attack of 5° , Reynolds number $Re_c = \rho_\infty u_\infty c / \mu = 408000$ and Mach number $M = u_\infty / a_\infty = 0.4$ is presented next. The background grid uses $n_x \times n_y = 701 \times 351$ grid points, the embedded body fitted O-grid of the NACA profile consists of $n_s \times n_r = 961 \times 102$ grid points. In the near field $-1 \leq x/c \leq 3$ and $-1 \leq y/c \leq 1$ the compressible Navier-Stokes equations were solved. The data required on both grids is obtained via 4th-order Lagrange interpolation [6].

The extension of the domain into the acoustic far-field is established by solving the linearized Euler equations (LEE). This approach was already used by Freund et al. [9], in the context of jet flow acoustics a similar approach was followed by Bogey and Bailly [2], amongst others. Therefore, the fluctuating density and velocity components were stored for three grid lines (determining the interface) at the upper and lower boundary at $y = \pm 0.5c$. The time step size was kept the same and set to $\Delta t_{LEE} = 0.001 \approx 100 \Delta t_{LES}$. The LEEs were discretized using a standard central difference scheme of sixth order, time integration was performed using a low-storage Runge-Kutta Scheme of third order after Williamson [20]. To minimize spurious waves the number of grid points and grid stretching in x -direction was chosen to be the same in both domains. The LEE-grid uses an uniform grid in y -direction, with grid spacing equal to the average of the interface grid size. Tam and Webb's [17] radiation boundary condition calculated using central and one-sided difference of fourth order were implemented at the boundaries. The origin of the source region required in this boundary condition, $\mathbf{r}_e = \mathbf{x} - \mathbf{x}_{ref}$, is located in the LES-domain and was chosen to be $\mathbf{x}_{ref} = (1, 0)$. Additional stabilisation is introduced automatically via the direct-filtering LES model, by filtering the solution each time step using a filter of 6th-order [8, 18]. Close to the outflow boundary at $x = 2c$ and the side boundaries at $y = \pm 0.6c$ a sponge layer is added via $-\sigma(q - q_0)$, using the mean field q_0 of

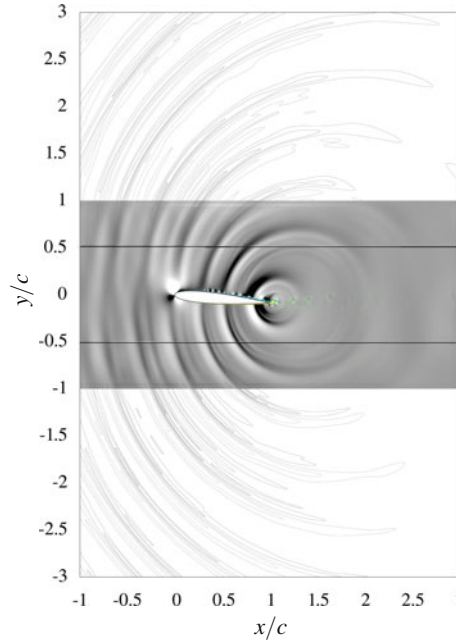


Fig. 3 2D NACA0012: Dilatation at time $t = 45c/a_\infty$ with continuous color scale between $\pm 0.1a_\infty/c$ within the LES area and 10 contour levels within the LEE area. Contour levels of the vorticity are shown between $\omega_z = -87a_\infty/c$ (blue) and $\omega_z = 87a_\infty/c$ (red), increment: $4a_\infty/c$. The interfaces are located at $y = \pm 0.5c$, indicated by the *black lines*

the quantity q [8, 15]. All calculations are performed dimensionless with reference values $\rho_\infty, a_\infty, a_\infty^2 \rho_\infty$ for density, velocity and pressure, as well as length scale c .

Figure 3 shows the instantaneous dilatation field of the LES and LEE simulation. The contour levels show a smooth transition from the LES to the LEE domain, with a mean flow of $(\rho_0, u_0, v_0) = (1, 0.4, 0)$, without significant numerical artefacts like spurious waves or reflections from the LEE domain boundaries. The density distribution along the x -axis at $y \approx -0.6c$ is shown in Fig. 4. Both curves are in good agreement. The distribution of the pressure coefficient, $-C_p = (p_\infty - \bar{p})/(0.5\bar{\rho}u_\infty^2)$, along the airfoil chord, shown in Fig. 5 (left), is in good agreement with the solution obtained by XFOIL assuming a viscous flow. The difference at the suction side is due to the boundary layer development at $x \approx 0.3c$, the difference at $x \approx c$ is due to the rounded trailing edge and observed separation bubble, as shown in figure on the right. This and further test cases (not shown here) were used to verify the LES procedure to predict the flow properties with high accuracy.

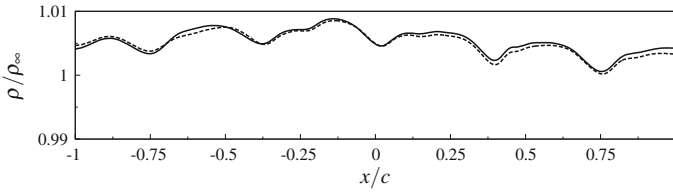


Fig. 4 2D NACA0012: density at time $t = 45c/a_\infty$ along x at $y \approx -0.6c$. —, LES, - - -, LEE

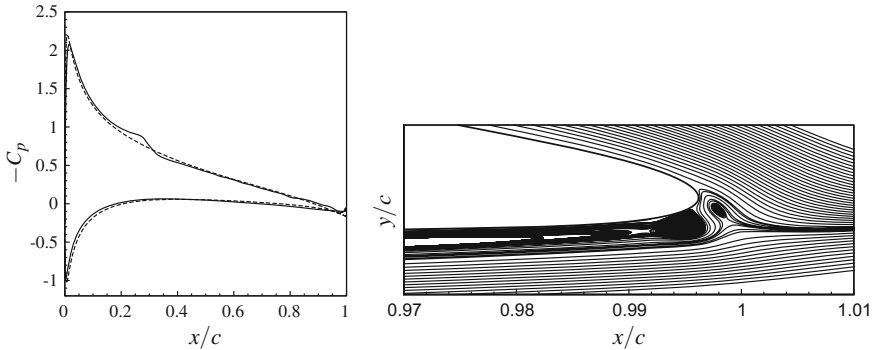


Fig. 5 2D NACA0012: *Left* Profile of the pressure coefficient $-C_p = (p_\infty - \bar{p})/(0.5\bar{\rho}u_\infty^2)$: —, LES, - - - XFOIL. *Right* Streamlines of the mean flow (\bar{u}, \bar{v})

3 Results

Since the simulation of the 3D jet-wing-flap configuration is very challenging, fundamental studies were performed first, using two-dimensional test cases originating from the planned configuration. The flow parameters of the test cases are identical to the final configuration, but reduce computational time significantly. Figure 6 shows an instantaneous view on the acoustic field of the 2D jet-wing-flap simulation. The acoustic field, visualized by divergence of the velocity, shows dominant noise sources in the exit region of the primary nozzle and smaller acoustic sources further downstream in the region where mixing layers merge. Moreover two smaller sound sources in the wing-flap gap area and at the flap trailing edge are observed.

Due to the input of momentum by the jet, strong boundary layer vorticity on the lower wing side develops, as demonstrated in Fig. 7. This leads to a significantly changed mean flow, too, shown in Fig. 8. In the case of an isolated airfoil, three recirculation areas are found in the gap (Fig. 8a), while in the entire configuration only one large recirculation area can be observed (Fig. 8b). As a result of the changed flow features, a reduced input of momentum occurs on the upper side of flap, the negative pressure on the upper side drops as shown by $-C_p$ in Fig. 9b. Additionally, the stagnation point shifts from the flap leading edge to its lower surface. This results in a spatially expanded high pressure region compared to the case without nozzle

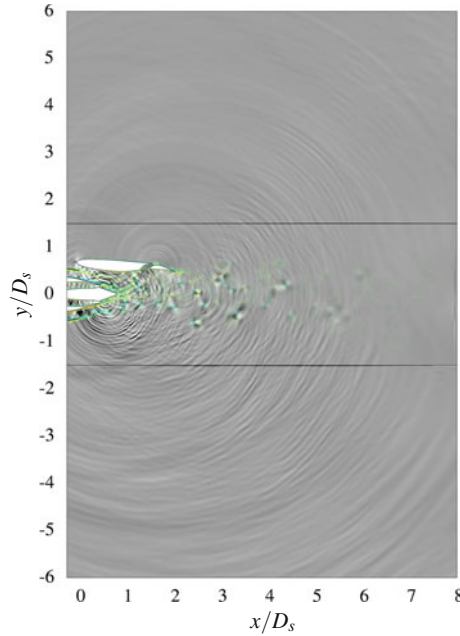


Fig. 6 2D wing with nozzle: Dilatation, $\nabla \cdot \mathbf{u}$, with continuous color scale between $\pm 0.1U_s/D_s$. Contour levels of the vorticity are shown between $\omega_z = -87U_s/D_s$ (blue) and $\omega_z = 87U_s/D_s$ (red), increment: $4U_s/D_s$. The interfaces are located at $y = \pm 1.5D_s$, indicated by the black lines



Fig. 7 2D wing without (left) and with nozzle (right). Contour levels of the vorticity magnitude $|\omega_z|$. The grey scale ranges from 0 up to the level of $50U_s/D_s$, from white to black

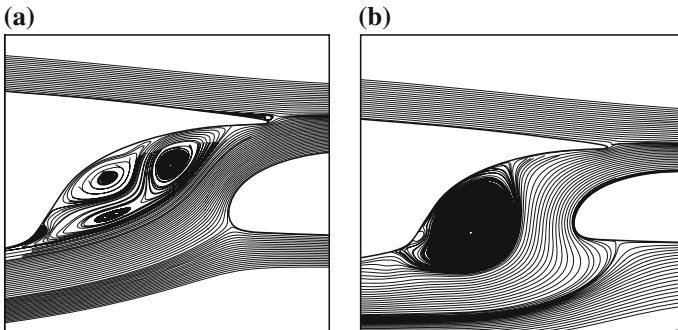


Fig. 8 2D wing without nozzle (a) and with nozzle (b): Streamlines of the mean flow

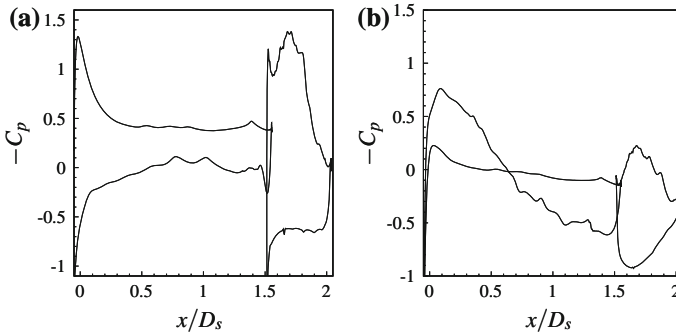


Fig. 9 Distribution of $-C_p$ along the 2-D wing chord: **a** without nozzle, **b** with nozzle

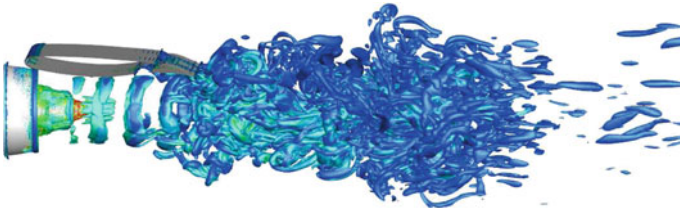


Fig. 10 3D jet-wing-flap configuration with $U_\infty = 0.467U_s$: Isosurfaces of $\lambda_2 = -1$ colored by vorticity magnitude, ranging from 0 up to $40 U_s/D_s$, from blue to red

(Fig. 9a). In Fig. 10, the λ_2 isosurfaces of the 3D jet-wing-flap configuration with $U_\infty = 0.467U_s$ are shown, the color scale corresponds to the vorticity magnitude. The shear layers of the jet interact with the flap trailing resulting in an immediate potential core breakdown. This is further discussed by looking at Fig. 11. The snapshots of the vorticity magnitude in the (y, z) -plane at $x = 1.5D_s$ and $x = 2D_s$ show the influence of the flap on the shear layer development. Without coflow (top row), additional weak vorticity shed from the wing due to entrainment interacts with the jet from above. Furthermore, the development of secondary vortices is inhibited on top and asymmetries develop, leading to a departure from a round jet development. This difference shrinks further downstream. For non-zero free-stream velocity (bottom row), the linear growth rate of the jet decreases and boundary layer vorticity interacts with the upper part of the jet. A spanwise region of vorticity close to the wing develops, with the vorticity directly on top of the jet interacting with the jet vorticity, being partly entrained by the latter. Close to the wing and sideways of the jet where the effects of entrainment are lower, two larger localized regions of vorticity develop, trailing behind the wing subsequently. The magnitude of the jet vorticity is clearly stronger in this case, compared to the case with zero free stream velocity. Furthermore the anisotropic shape of the vortical structures is more noticeable. It should be noticed, that further statistical analysis will be needed and is currently



Fig. 11 3D jet-wing-flap configuration with $U_\infty = 0$ (top) and $U_\infty = 0.467U_s$ (bottom): Snapshots of vorticity magnitude in the (y, z) -planes at $x = 1.5D_s$ and $3.75D_s$ (left); at $x = 2D_s, 4D_s$ and $6D_s$ (right). The grey scale ranges from 0 up to the level of $15U_s/D_s$, from white to black

being performed to analyse the differences in detail. Additionally, comparisons with the single jet and with cases for different flap angles are currently simulated.

4 Conclusions

Preliminary results obtained through LES simulations of a 2D and 3D jet-wing-flap configuration were performed. Initial results have shown, that the jet leads to a significant change of the flow and pressure fields close to and at the wing surface, with strong influence on the radiated sound. Furthermore, the coflow strongly influences the vortical structures. In the near future a detailed analysis will be conducted including the balance of the Reynolds stresses, turbulent kinetic energy, the length scales and the invariants of the velocity gradient tensor. Additionally, the influence of the coflow, jet temperature, wing position and flap angle on the acoustic source terms and the radiated sound field will be investigated in more detail and compared with experimental data.

Acknowledgements This work was supported by Airbus Group SE and through the LuFoV-1 project LIST under grant number 20T1307D. The authors thanks Dr. Daniel Redmann and Jörgen Zillmann of the Airbus Group SE for kindly providing the geometric data, as well as Tobias Gütelhöfer for his work on the LEE farfield solver.

References

1. Andersson, N., Eriksson, L.-E., Davidson, L.: LES prediction of flow and acoustic field of a coaxial jet. In: Proceedings of the 11th AIAA/CEAS Aeroacoustics Conference, AIAA Paper 2005-3043, Monterey, California, May 2005
2. Bogey, C., Bailly, C.: Influence of nozzle-exit boundary-layer conditions on the flow and acoustic fields of initially laminar jets. *J. Fluid Mech.* **663**, 507-538 (2010)
3. Bogey, C., Barré, S., Juvé, D., Bailly, C.: Simulation of a hot coaxial jet: Direct noise prediction and flow-acoustics correlations. *Phys. Fluids* **21**, 035105 (2009)
4. Bogey, C., Marsden, O., Bailly, C.: Influence of initial turbulence level on the flow and sound fields of a subsonic jet at a diameter-based Reynolds number of 10^5 . *J. Fluid Mech.* **701**, 352-385 (2012)
5. Bühler, S., Kleiser, L., Bogey, C.: Simulation of subsonic turbulent nozzle jet flow and its near-field sound. *AIAA J.* **52**, 1653-1669 (2014)
6. Chesshire, G., Henshaw, W.D.: Composite overlapping meshes for the solution of partial differential equations. *J. Comput. Phys.* **90**, 1-64 (1990)
7. Eschricht, D., Yan, J., Michel, U., Thiele, F.: Prediction of jet noise from a coplanar nozzle. In: Proceedings of the 14th AIAA/CEAS Aeroacoustics Conference, AIAA Paper 2008-2969, Vancouver, British Columbia Canada, May 2008
8. Foysi, H., Mellado, M., Sarkar, S.: Simulation and comparison of variable density round and plane jets. *Int. J. Heat Fluid Flow* **31**, 307-314 (2010)
9. Freund, J.B., Lele, S.K., Moin, P.: Matching of near/far-field equation sets for direct computations of aerodynamic sound. In: Proceedings of the 15th AIAA Aeroacoustics Conference, AIAA Paper 93-4326, Oct 1993
10. George, K.J., Lele, S.K.: Large eddy simulation of airfoil self-noise at high Reynolds number. In: Proceedings of the 22nd AIAA/CEAS Aeroacoustics Conference, AIAA Paper 2016-2919, Lyon, France, June 2016
11. Georgiadis, N.J., DeBonis, J.R.: Navier-stokes analysis methods for turbulent jet flows with application to aircraft exhaust nozzles. *Prog. Aerosp. Sci.* **42**, 377-418 (2006)
12. Henshaw, W.D.: OverBlown: A Fluid Flow Solver for Overlapping Grids, Reference Guide, Version 1.0. Centre for Applied Scientific Computing, Lawrence Livermore National Laboratory, Livermore, California (2003)
13. Jameson, A.: Numerical Methods in Fluid Dynamics. Springer (1983)
14. Kim, D., Lee, G.-S., Cheong, C.: Inflow broadband noise from an isolated symmetric airfoil interacting with incident turbulence. *J. Fluid Struct.* **55**, 428-450 (2015)
15. Marinc, D., Foysi, H.: Investigation of a continuous adjoint-based optimization procedure for aeroacoustic control of plane jets. *Int. J. Heat Fluid Flow* **38**, 200-212 (2012)
16. Neitfeld, A., Boenke, D., Dierke, J., Ewert, R.: Jet noise prediction with eddy relaxation source model. In: Proceedings of the 21st AIAA Aeroacoustics Conference, AIAA Paper 2015-2370, June 2015
17. Tam, C.K.W., Webb, J.C.: Dispersion-relation-preserving finite difference schemes for computational acoustics. *J. Comput. Phys.* **107**, 262-281 (1993)
18. Vasilyev, O.V., Lund, T.S., Moin, P.: A general class of commutative filters for LES in complex geometries. *J. Comput. Phys.* **146**, 82-104 (1998)
19. Vuillemin, A., Loheac, P., Rahier, G., Vuillot, F., Lupoglazoff, N.: Aeroacoustic numerical method assessment for a double stream nozzle. In: Proceedings of the 11th AIAA/CEAS Aeroacoustics Conference, AIAA Paper 2005-3043, Monterey, California, May 2005
20. Williamson, J.H.: Low-storage runge-kutta schemes. *J. Comput. Phys.* **35**, 48-56 (1980)
21. Wolf, W.R., Lele, S.K.: Trailing-edge noise predictions using compressible large-eddy simulation and acoustic analogy. *AIAA J.* **50**, 2423-2434 (2012)
22. Xia, H., Tucker, P.G., Eastwood, S.: Large-eddy simulations of chevron jet flows with noise predictions. *Int. J. Heat Fluid Flow* **30**, 1067-1079 (2009)